IUCrJ
ISSN 2052-2525
ELECTRON CRYSTALLOGRAPHY

Round robin on structure analysis from 3D electron diffraction data

Mauro Gemmi,[a]* Lukáš Palatinus,[b] Philippe Boullay,[c] Jan Pieter Abrahams,[d,e] Amatassalâm Ben Meriem,[d] Erica Cordero-Oyonarte,[c] Vincentia Emerson Agbemeh,[a] Hrushikesh Chintakindi,[a] Moussa Diame Faye Diouf,[a] Pavel Filipcik,[e] Laura Gemmrich Hernandéz,[f] Eric van Genderen,[e] Joke Hadermann,[g] Amirhossein Hajizadeh,[g] Branislav Jeriga,[h] Ute Kolb,[f] Senik Matinyan,[d] Sara Passuti,[c] Marco Santucci,[f] Ashwin Suresh,[b] Olivier Pérez,[c] Cheuk-Wai Tai,[h] Angelina Vypritskaia,[h] Lei Wang,[h] Hongyi Xu[h] and Xiaodong Zou[h]

[a]Electron Crystallography, Center for Materials Interfaces, Istituto Italiano di Tecnologia, Viale Rinaldo Piaggio 34, Pontedera, Italy, [b]Institute of Physics of the Czech Academy of Sciences, Prague, Czechia, [c]CRISMAT, CNRS, Normandie University, ENSICAEN, UNICAEN, 14000 Caen, France, [d]Biozentrum, University of Basel, Basel, Switzerland, [e]Laboratory of Nanoscale Biology, Paul Scherrer Institute, Villigen, Switzerland, [f]Institute for Inorganic Chemistry and Analytical Chemistry, Johannes Gutenberg-University, 55128 Mainz, Germany, [g]EMAT, Department of Physics, University of Antwerp, 2020 Antwerp, Belgium, and [h]Department of Materials and Environmental Chemistry, Stockholm University, Stockholm SE-106, Sweden. *Correspondence e-mail: mauro.gemmi@iit.it

Received 29 September 2025
Accepted 16 January 2026

Edited by L. Meshi, Ben-Gurion University of the Negev, Israel

Keywords: electron diffraction; electron microscopy; dynamical refinement; 3D ED.

CCDC references: 2528653–2528693

Supporting information: this article has supporting information at www.iucrj.org

3D electron diffraction (3D ED) has undergone impressive development in the last decade. However, its accuracy and reproducibility have never been tested, up to now, in different laboratories on the same batch of samples. This paper reports a round robin on three test structures, two inorganic and one organic, solved and refined with 3D ED in seven different laboratories employing different transmission electron microscopes, with different acceleration voltages, different methodologies and different detectors. The results of the round robin show a remarkable accuracy of the technique that, in the case of kinematical refinement, is around 0.05 Å error on atomic positions for the inorganic samples and 0.15 Å for the beam-sensitive organic crystal. Dynamical refinement further improves the accuracy. The analysis of diverse samples and numerous data sets again confirms that dynamical refinement is a well established procedure, significantly reducing the refinement *R* factors, improving the accuracy of the structure models in most cases, and providing fine structural details, such as hydrogen-atom positions and the absolute structure, for both inorganic and organic samples.

1. Introduction

3D electron diffraction (3D ED) has undergone incredible development in the last two decades (Gemmi *et al.*, 2019). From a niche technique used in a few laboratories, it has become one of the major new developments in crystallography to be considered for the technique of the year by the journal *Science* in 2018 (Service, 2018). All started in 2007, when Kolb *et al.* proposed the collection of a sequence of still patterns separated by 1° of tilt, avoiding any zone axis orientation, then reconstruction of the reciprocal space offline on a PC after the end of the experiment (Kolb *et al.*, 2007). From this 3D reconstructed volume, the unit-cell parameters could be determined, and the reflections could be indexed and integrated. The next milestone in the technique was the proper integration of the reflection intensity over the excitation error, avoiding the missing wedge between the collected patterns. This was achieved initially by collecting the patterns in precession mode (the PEDT technique; Mugnaioli *et al.*, 2009)

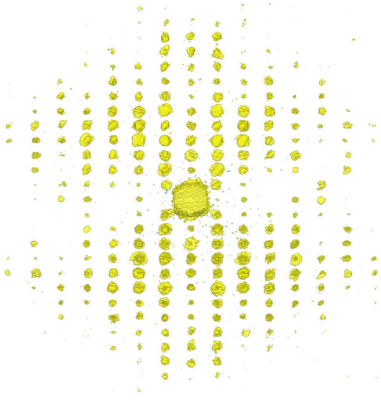

and later by collecting them while the crystal is rotating, the so-called cRED or microED technique (Nederlof *et al.*, 2013; Nannenga *et al.*, 2014; Gemmi *et al.*, 2015). The reflection intensities of PEDT and cRED, if interpreted as the square moduli of the structure factors (kinematical approximation), can be successfully used for solving the crystal structure, making 3D ED a single-crystal diffraction technique for nanocrystals. The final step was to provide a refinement procedure based on the physical principles of electron scattering (Bloch-wave solution of the Schrödinger equation), taking into account dynamical scattering effects that influence diffracted intensities. These refinements, distinct from those based on the kinematical approximation (kinematical refinements), are referred to as dynamical refinements. This approach enabled the refinement of a crystal structure with an accuracy comparable to that of X-ray diffraction, thereby advancing 3D ED toward the reliability of single-crystal X-ray diffraction in the refinement of atomic parameters. Dynamical refinement of crystal structures using 3D ED data was successfully demonstrated for PEDT in 2015 (Palatinus *et al.*, 2015*a*; Palatinus *et al.*, 2015*b*) and for cRED in 2023 (Klar *et al.*, 2023).

Many limitations on the type of samples that can be investigated by 3D ED have also now been overcome. Like the cryo-EM technique, 3D ED performance spiked thanks to the development of new single-electron detectors (Nederlof *et al.*, 2013; Tinti *et al.*, 2018), which allow experiments under very low dose conditions. This, together with dedicated sample preparation methods like low-temperature measurements or cryo-protection, has extended the application of 3D ED to beam-sensitive materials like organics and macromolecules. The remarkable results obtained with electrons have also triggered the development of instruments dedicated to 3D ED which are veritable electron diffractometers (Ito *et al.*, 2021; Simoncic *et al.*, 2023). We can therefore affirm that from macro- to nanocrystals, nowadays we have single-crystal diffraction techniques able to determine the crystal structure, with the boundary between the choice of X-ray or electrons lying somewhere in the one-micron range.

With 3D ED exiting its infancy, it is now time to test the technique in different laboratories to check the reproducibility of the results and their typical accuracy. This objective was achieved as part of the collective training of the PhD students involved in the H2020 MSCA-ITN *Electron Nanocrystallography* project (GA 956099). Three different crystalline samples were selected, each presenting its own specific challenges, and distributed among seven laboratories, without any information on their chemical nature, which should be derived through energy dispersive X-ray spectroscopy. The laboratories' task was to solve their structures and try to refine the structure models at the maximum possible accuracy. This is the first time that such an experiment has been attempted, and it is thus a unique opportunity to test at which level 3D ED can be considered reliable and reproducible. Different TEMs, mainly, but not only, specialized for 3D ED data acquisition, were employed across a relatively broad range of technical parameters (acceleration voltages, gun sources, detectors) to conduct the round-robin experiments. Some laboratories have used PEDT setups, others cRED. Both the data reduction and the data analysis were carried out using different software. We

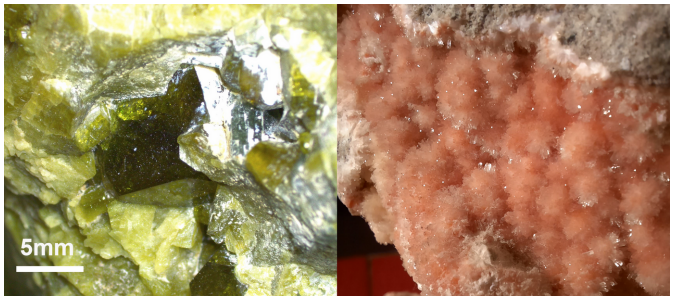

Figure 1
(Left) Picture of the crystal of epidote that was crushed for the round robin. (Right) Sample of natrolite from which the crystals for the round robin were taken. The scale bar applies to both images.

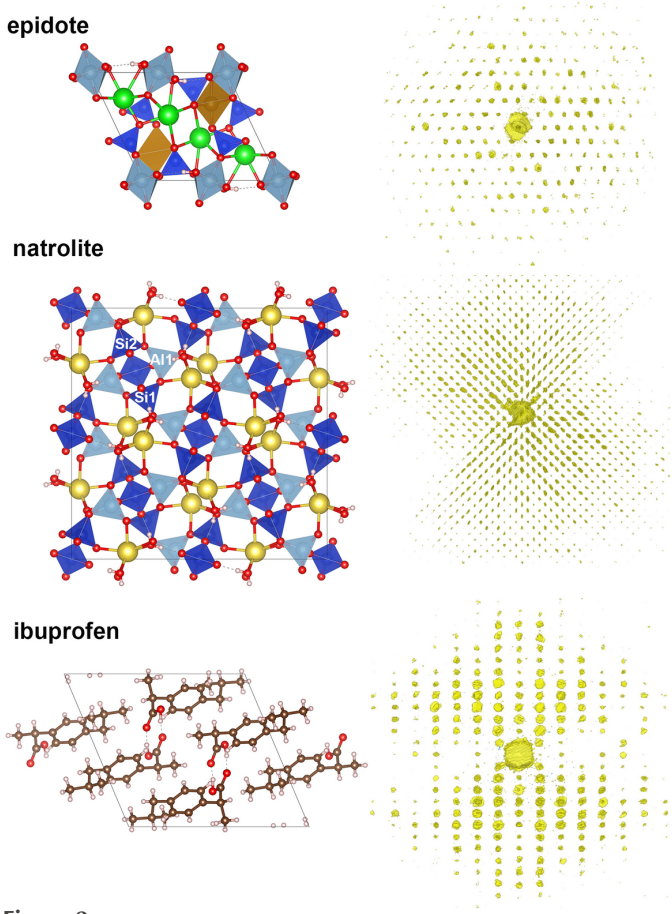

Figure 2
Top: crystal structure of epidote viewed along **b** and its reconstructed reciprocal space viewed along (010) in a PEDT experiment. Colour code: Al light blue, SiO_4 tetrahedra blue, Al/Fe polyhedra brown, Ca green, O red and H white. Centre: the natrolite crystal structure viewed along **c** and its reconstructed reciprocal space viewed along (001) in a cRED experiment. Atom colour code: Si blue, Na yellow, Al light blue, O red, H white. The labelling of the three non-equivalent tetrahedral sites is highlighted. Bottom: the *S*-ibuprofen crystal structure viewed along **b** and its reconstructed reciprocal space viewed along (100) in a cRED experiment. Atom colour code: O red, C brown, H white.

Table 1
Experimental setups of the different laboratories involved in the round robin.

The beam size in the case of the SAED experiment represents the apparent diameter of the SAED diaphragm in the image plane. NBED – nanobeam electron diffraction. SAED – selected area electron diffraction. HT is the acceleration voltage of the TEM.

Lab	TEM	HT (kV)	Technique	Detector	Illumination	Operation mode	Beam size (μm)
1	Zeiss Libra 120	120	PEDT/cRED	Timepix1	NBED	STEM	0.15/0.15
2	Fei Tecnai G2	200	cRED	Timepix1	NBED	TEM	0.5
3	Fei Tecnai G2 20	200	PEDT/cRED	Medipix3	NBED	TEM	between 1.0 and 1.8
4	Fei Tecnai F30 STWIN	300	PEDT	Ultrascan 4000	NBED	STEM	0.2
5	JEOL 2100	200	cRED	Timepix1	SAED	TEM	1.6
6	JEOL F200	200	PEDT/cRED	Medipix3	NBED	TEM	0.075/2.0
7	JEOL F200	200	cRED	Medipix3	NBED	TEM	0.5

can affirm that the results of this survey provide a complete panorama of how 3D ED can tackle the structure determination of an unknown structure.

2. Experimental methods

2.1. Test structures

The selected test structures are two inorganic minerals, epidote and natrolite, and one organic beam-sensitive sample, the drug ibuprofen. As inorganic samples, we selected two highly crystalline mineral samples to avoid problems connected to the crystal size or to crystal imperfections, so that all the challenges came from the peculiarities of the crystal structures. In contrast, the organic sample was selected to be a rather challenging case, in which the beam sensitivity pushes the requirements on the experimental setup and data collection strategy to the limits.

2.1.1. Epidote, $Ca_2Al_2(Fe^{3+},Al)(SiO_4)(Si_2O_7)O(OH)$

Epidote is a silicate mineral belonging to the sorosilicate family, as it contains $(Si_2O_7)^{6-}$ groups in its structure. The sample used in the round robin was obtained by crushing one macro-crystal (Fig. 1) of a natural epidote from Val d'Ossola, Italy. The epidote structure (Fig. 2, top) is monoclinic, space group $P2_1/m$, with 19 atoms in the asymmetric unit (Dollase, 1971). The biggest challenges in the structure determination of epidote are:

(*a*) direct detection and possible refinement of the hydrogen atom present in the structure, and

(*b*) the presence of a site with a mixed Al/Fe occupancy to be refined.

2.1.2. Natrolite, $Na_2Al_2Si_3O_{10}\cdot 2H_2O$

Natrolite is a tectosilicate mineral belonging to the zeolite family. Its structure is formed by a three-dimensional network of $(SiAl)O_4$ tetrahedra, hosting Na and coordinated water in the channels. Small batches of the same natrolite sample (Fig. 1) were shared among the laboratories. The sample is a natural natrolite from Marianska Skala, Usti nad Labem, Czechia. The natrolite structure (Fig. 2, centre) is orthorhombic, space group *Fdd*2, with 12 atoms in the asymmetric unit (Meier, 1960). The biggest challenges of its crystal structure analysis are:

(*a*) correctly determining the symmetry, which is orthorhombic but pseudotetragonal;

(*b*) distinguishing the Al tetrahedra from the Si tetrahedra by comparing the cation–oxygen distances;

(*c*) determining the hydrogen-atom positions of the water molecules; and

(*d*) determining the absolute structure, since natrolite is not centrosymmetric.

2.1.3. Ibuprofen, $C_{13}H_{18}O_2$

Ibuprofen is a well known nonsteroidal anti-inflammatory drug. The ibuprofen molecule is chiral, and it can form a centrosymmetric crystal structure in the space group $P2_1/c$ with both enantiomers present (McConnell, 1974) or a non-centrosymmetric crystal structure in the space group $P2_1$ containing either only left- (*S*-) or right-handed (*R*-) molecules, *i.e.* just one enantiomer present (Freer *et al.*, 1993) (Fig. 2, bottom). For our test, we selected an enantiopure powder of *S*-ibuprofen bought from Sigma Aldrich at 99% purity, with the specific aim of verifying the determination of the absolute structure of an organic sample. The challenges presented by the *S*-ibuprofen samples were:

(*a*) the vacuum and beam sensitivity of ibuprofen, which sublimates in the TEM vacuum, requiring the use of a cryo-holder and a low-dose data collection setup;

(*b*) determining the positions of the hydrogen atoms, which can be particularly challenging; and

(*c*) determination of the absolute structure.

2.2. Instruments and data collection types

The round robin experiments exhibit a remarkable variability in the TEM types, data collection modes and voltages, covering a representative ensemble of experimental configurations typically used in 3D ED (see Table 1). Three different high voltages have been used: 120, 200 and 300 kV; five different instruments: an FEI Tecnai G2 20, an FEI Tecnai F30, a JEOL 2100, a JEOL F200 and a Zeiss Libra 120, some with thermionic sources and some with FEG sources. Two of these instruments, the FEI Tecnai F30 and Zeiss Libra 120, were operated in STEM mode, while the others were used in TEM mode. Details of the 3D ED data collection in the different laboratories are provided in Tables S1, S2 and S3 in

the supporting information for epidote, natrolite and *S*-ibuprofen, respectively.

In terms of data collection type, two different approaches were used based on their ability to yield 3D ED data sets suitable for both kinematical and dynamical refinements:

(1) PEDT: precession-assisted 3D ED (Mugnaioli *et al.*, 2009), in which the data collection is carried out with sequential and discrete tilt steps with the beam precessing on a cone (precession electron diffraction; Vincent & Midgley, 1994). The selected cone semi-apertures ranged from 1° to 1.4°.

(2) cRED: continuous rotation 3D ED (Nederlof *et al.*, 2013; Nannenga *et al.*, 2014; Gemmi *et al.*, 2015), in which the patterns are collected during the crystal rotation. In this case, the tilt step is determined by the detector exposure time, which directly integrates the diffraction intensities during the rotation. If ω is the angular speed of the goniometer and t_{exp} is the exposure time, the angular step is given by ωt_{exp}. This technique is the closest to the conventional rotation technique in single-crystal X-ray diffraction.

These two approaches are currently the most widely used, each for different reasons. For a long time, PEDT was the only method capable of providing data suitable for dynamical refinement and was favoured by laboratories aiming for accurate structural analysis. cRED, on the other hand, was developed more recently than PEDT to acquire very fast 3D ED data from beam and/or vacuum-sensitive materials and, until recently, was primarily used on organics for structure solution and kinematical refinement. With the advent of dynamical refinement using cRED data (Klar *et al.*, 2023) and of dedicated electron diffractometers (Ito *et al.*, 2021; Simoncic *et al.*, 2023) that work exclusively in cRED mode, the application of this method is expanding. The characteristics of the investigated material determine the preferred data collection type. However, the possibility of using one or the other approach also depends on the instrument and its equipment, such as the presence of a precession module, the stability of the goniometer, the detector and other factors.

Most of the 3D ED data used for the structure solution and refinement were obtained from a single crystal, with the angular data collection range varying from 60° to 130°. When a single data set does not provide enough reciprocal-space coverage, multiple data sets can be merged. This is crucial for enhancing the likelihood of success in the structure solution stage and, as will be discussed later, may also be beneficial in the structure refinement stage. This strategy was employed by one laboratory for the epidote sample and by three laboratories for the ibuprofen sample.

The illumination of the samples was of two types:

(1) NBED, nanobeam electron diffraction: the whole crystal or part of it was illuminated by a parallel nanobeam; or

(2) SAED, selected area electron diffraction: the diffracted area was selected through an aperture placed in the image plane (SAED diaphragm).

In terms of detectors, two types were used: CCDs and single-electron-counting hybrid pixel detectors (HPDs). In the case of CCDs, a Gatan Ultrascan 4000 was the only model used in this study. Both the HPDs that were used were produced by ASI, and they were the Timepix1 and Cheetah M3 based on Medipix3 technology. Both HPDs were 512 × 512 pixels.

The sample preparation for the two inorganic samples was the same in all laboratories: the crystals were crushed in an agate mortar and were dispersed on a holey carbon grid using a polar liquid, like ethanol or isopropanol. The *S*-ibuprofen samples had to be prepared dry to avoid dissolution. The grid was prepared by touching it onto a powder dispersed on a flat surface or by dipping the grid directly into the powder, exploiting the adhesion through surface forces of the small crystals to the holey carbon film.

Data for the *S*-ibuprofen samples were measured with the help of a cryo-holder at temperatures around −170°C.

Examples of data collections on the different samples can be found in Fig. 2, where projections of the three-dimensional reconstruction of the reciprocal space, visualized using the software *VESTA* (Momma & Izumi, 2011), are displayed.

2.3. Data reduction

The treatment of the 3D ED data can be divided into two steps. Data reduction, in which the raw data are processed to obtain the unit-cell parameters, index the reflections and extract their intensities; and data analysis, in which a structural model is derived from the extracted intensities and subsequently refined.

For the data reduction, three main programs were used: *PETS2*, *XDS* and *DIALS*, which are briefly described in the following.

PETS2 (*Process Electron Tilt Series*, version 2) is a computer program intended for processing 3D ED data from a series of diffraction patterns (Palatinus *et al.*, 2019). The program allows the user to create a list of peak coordinates by peak hunting from the diffraction patterns. This can then be used to find the orientation matrix and to determine the lattice parameters. The program also enables correction of geometric distortions arising from TEM optics (Brázda *et al.*, 2022) and ED frame misorientations. *PETS2* uses the orientation matrix to integrate the diffracted intensities for kinematical and dynamical refinement (Palatinus *et al.*, 2015*a*; Palatinus *et al.*, 2015*b*). A rocking curve is displayed at the end of the integration process. The rocking curve width ($Å^{-1}$) and the apparent mosaicity (°) are the two main profile parameters of the rocking curve used for integration. Once the integration is finalized, the program produces a normal distribution plot for $\sigma(I)$ values, which the user can adjust and refine by using an error model to correct the $\sigma(I)$ values (Khouchen *et al.*, 2023). An intensity statistic is also generated for each Laue class and each resolution shell for the preferred Laue class. Finally, the software creates three output files: `name.hkl` [which contains a list of reflections *hkl* with intensity and $\sigma(I)$ values; this can be used by any software that uses the kinematical approximation for refinement and structure solution], `name.cif_pets` (a reflection file for kinematical refinement in CIF format, readable by *Jana2006*/*2020*) and

name_dyn.cif_pets (the reflection file for dynamical refinement in *Jana2006/2020*). The program can also be used for the calculation of arbitrary 2D sections of reciprocal space, the calculation of the 3D reconstruction of the intensity distribution in reciprocal space and for the processing of data from modulated crystals.

XDS (*X-ray Detector Software*; Kabsch, 2010), is a software package originally designed for processing single-crystal diffraction data collected via the rotation method with monochromatic X-rays, but it is also able to process cRED data with some minor adjustments. *XDS* handles diffraction data through a modular approach, dividing data reduction into several tasks specified in the XDS.INP file. The XDS.INP file is the only input file required to run *XDS* and contains all the necessary information to process a data set. This includes details such as the image data and the format, the geometry, the calibrations, and other experimental parameters. The JOB keyword within this file defines the sequence of tasks, such as XYCORR, INIT, COLSPOT, IDXREF, DEFPIX, INTEGRATE and CORRECT. Each task produces an output file (<TASK>.Lp), which serves as the input for the subsequent task.

The first tasks in *XDS* are XYCORR and INIT. The XYCORR task generates lookup tables that apply spatial corrections to detector pixel positions, ensuring their accurate mapping into the laboratory coordinate system. These corrections can be particularly relevant when distortions are present, especially in high-symmetry space groups. Meanwhile, the INIT task produces background noise and pixel gain maps, along with initial estimates of the background at each pixel, which are essential for distinguishing between background and signal pixels in subsequent steps.

The next steps include COLSPOT and IDXREF. The COLSPOT task identifies strong diffraction spots in the images and stores their centroids, which are then read by IDXREF to determine the crystal lattice parameters and orientation. While *XDS* can attempt to guess the symmetry, it is often necessary to manually select a unit cell from the proposed list and assign a space group, making sure that the Laue class is correct, before re-running the IDXREF task.

The final stages of data processing are handled by DEFPIX, INTEGRATE and CORRECT. DEFPIX is responsible for masking invalid regions of the detector, such as shadows or unexposed areas, making sure that only reliable data are included for the intensity extraction. The INTEGRATE task then calculates the intensities of the reflections using the refined orientation matrix and experimental geometry to predict reflection positions in detector and rotation space. For each reflection, a local background is estimated and subtracted, and integrated intensities are determined primarily by three-dimensional profile fitting, in which an empirical reflection profile derived from strong reflections is fitted to individual observations. When profile fitting is not applicable, summation of background-corrected pixel values is used. The resulting intensities are written to the INTEGRATE.HKL file. Finally, the CORRECT task performs scaling of the integrated intensities, rejects outliers, computes statistical parameters and produces the final reflection data file, XDS_ASCII.HKL. Throughout these steps, the *XDS* configuration file (XDS.INP) is adjusted to optimize processing parameters, and the entire procedure or individual tasks can be repeated iteratively.

DIALS (*Diffraction Integration for Advanced Light Sources*) is software originally developed for single-crystal X-ray data analysis by Diamond Light Source, Lawrence Berkeley National Laboratory and CCP4 (Winter *et al.*, 2018) which offers a set of tools well suited for electron diffraction data (Clabbers *et al.*, 2018; Vypritskaia *et al.*, 2025). The version used here was 3.10 with manual specification of experimental geometry.

The software uses the same general workflow as *XDS*, with individual steps launched from the command line and two graphical tools to inspect the results of each step visually – *dials.image_viewer* and *dials.reciprocal_lattice_viewer* for real space and reciprocal space, respectively. *DIALS* imports experimental data and metadata, finds strong reflections in the data set, and indexes the reflections, initially always on a primitive lattice. Then the data set is checked for consistency with each possible Bravais lattice and reindexed in the best-fitting configuration. Further refinement in the best-fitting Bravais lattice updates the input experimental geometry parameters, as well as the determined unit-cell parameters. Based on the refined unit-cell parameters, *DIALS* predicts spot locations throughout the data set and integrates the measured intensities using summation or profile fitting in 3D. At this point, *DIALS* can make further checks for higher-symmetry groups using systematic absences, merge several data sets based on shared reflections, and scale the data sets together for internal consistency. Finally, *DIALS* exports a reflection file suitable for downstream structure solution. *DIALS* is fully modular, and the workflows can be iterated and tweaked as required, with many options at each step.

2.4. Structure analysis

Since the samples were provided without any chemical information, every laboratory obtained the chemical composition from energy dispersive X-ray spectroscopy (EDS) analysis and refined it through the structure analysis.

Three different programs were used for the structure solution: *SIR*, based on direct methods (*Sir2014/2019*; Burla *et al.*, 2015), *Superflip* (Palatinus & Chapuis, 2007) and *ShelxT* (Sheldrick, 2015*b*), both using dual-space iterative algorithms: charge flipping in the case of *Superflip*, and the so-called intrinsic phasing in the case of *ShelxT*. All programs treat the data based on a kinematical approximation, like in the case of X-ray diffraction, with the only caveat of selecting electron atomic scattering factors where applicable.

Structure refinements with 3D ED data are of two types: kinematical refinement, where the intensities are treated as proportional to the square moduli of the corresponding structure factors, and dynamical refinement, where the dynamical scattering is adequately modelled through Bloch-wave calculation. Dynamical refinement utilizes a more accurate

Table 2
Summary of the solution and refinement of the epidote structure.

In the last two rows, the average agreement factors and their standard deviations (Stdev.) are reported. Here and in the following tables: rows with labels ending in c are for cRED experiments, rows with labels ending in p are for PEDT experiments. Comp. (%) stands for percentage completeness.

Label	Lab	Data processing	Solution	Refinement	R_{int} (%)	Compl. (%), (resolution, Å)	Kinematical		Dynamical	
							R(obs)	*R*(all)	*R*(obs)	*R*(all)
e1p	1	*PETS2*	*Sir2019*	*Jana2020*	23.36	89 (0.77)	24.48	29.34	12.00	16.78
e2c	2	*PETS2*	*Superflip*	*Jana2020*	20.56	91 (0.45)	22.22	30.19	9.37	10.27
e3p	3	*PETS2*	*Superflip*	*Jana2020*	6.63	87 (0.50)	21.58	21.66	9.13	9.68
e3c	3	*PETS2*	*Superflip*	*Jana2020*	15.27	85 (0.50)	23.70	24.28	9.97	10.07
e4p	4	*eADT/PETS2*	*Sir2014*	*ShelxL* (kin)/*Jana2020* (dyn)	11.51	68 (0.71)	24.50	24.78	10.23	10.96
e5c	5	*REDp/XDS/Xscale*	*ShelxT*	*ShelxL*	23.34	97 (0.67)	17.49	18.71		
e6p	6	*PETS2*	*Superflip*	*Jana2020*	23.69	89 (0.56)	27.24	27.38	13.67	14.88
e7c	7	*DIALS*	*ShelxT*	*ShelxL*	13.87	83 (0.80)	21.75	24.55		
						Average	**22.87**	**25.11**	**10.72**	**12.11**
						Stdev.	**2.7**	**3.6**	**1.6**	**2.7**

modelling of the physical process of electron diffraction to compute the calculated intensities. However, it requires a very stable experimental setup and accurate data collection. For example, the modelling can be less accurate if the beam wanders over areas of different thicknesses during the data collection. Finally, dynamical refinement is a computationally demanding method, and while it is relatively quick on small structures, it can be very time consuming for large structures.

Since kinematical refinement is analogous to the refinement performed with X-ray data, all the software available for X-ray diffraction can be used successfully. In the round robin, the laboratories selected different software for kinematical refinements, namely *Jana2020* (Petříček *et al.*, 2023), *ShelxL* (Sheldrick, 2015*a*) and *OLEX2* (Dolomanov *et al.*, 2009). For dynamical refinements, the only software available at the moment is the program *Jana2020* combined with the Bloch-wave calculation software *Dyngo* (Palatinus *et al.*, 2015*b*). This software can perform dynamical refinement on both PEDT (Palatinus *et al.*, 2015*a*) and cRED data (Klar *et al.*, 2023).

In the following text we have used a special labelling scheme to identify each data set and the corresponding refined structures: for the data sets the label consists of three letters or numbers, the first one for the material (e for epidote; n for natrolite; i for ibuprofen), the second for the laboratory and the third one for the data collection type (c for cRED; p for PEDT); for the corresponding CIF files a string is added to identify the type of refinement ('kin' for kinematical; 'dyn' for dynamical).

3. Results

3.1. Solution and refinement

Both inorganic structures were successfully solved and kinematically refined by all laboratories. Interestingly, the *R*1 agreement factor of refinement is systematically lower for natrolite than epidote for all pairs of data sets coming from the same laboratory. *R*1(obs) for epidote varies between 17.5% and 27.2% with an average of 22.9% (Table 2), while for natrolite, it varies between 14.0% and 19.6% with an average of 15.7% (Table 3). Moreover, the lowest value of *R*1 achieved on the epidote sample coincides with the data set obtained by merging five different data sets (Table S1), indicating that merging is effective in reducing the dynamical scattering effects in the data.

Only five laboratories measured the *S*-ibuprofen structure owing to its beam sensitivity and tendency to sublimate in the TEM vacuum. It was completely impossible to collect data at room temperature, and only at −170 °C did the sample remain crystalline for the entire duration of one diffraction experiment, which was always performed in low-dose conditions. Regarding microscope operating modes, both cRED and PEDT modes were successfully used. The cRED technique in TEM mode allows for extremely rapid data acquisition (of the order of tens of seconds), significantly reducing total crystal exposure. Another approach involves using the microscope in STEM mode, which allows for reduced overall crystal illumination compared with the TEM mode. As a result, only the two laboratories operating in STEM mode successfully collected PEDT data on ibuprofen, achieving total collection times of a few minutes. In some of the data collections, it was impossible to cover a wide angular range in a single acquisition. For ibuprofen, half of the data sets that were used were obtained by merging data from several crystals (from 2 to 10, Table S3). The *S*-ibuprofen structure was solved *ab initio* and refined kinematically with *R*1(obs) varying between 15.9% and 22.8%, with an average of 19.68% (Table 4).

The dynamical refinement dramatically improves the agreement factors, as expected, and it allows all the characteristic challenges for these structures to be addressed. The inorganic structures were dynamically refined by five laboratories. *R*1(obs) for epidote varies between 9.1% and 13.7% with an average of 10.7%, while for natrolite, it varies between 5.7% and 13.6% with an average of 9.6% (Tables 2 and 3). The *S*-ibuprofen structure was refined dynamically by three laboratories (four data sets). In two cases data from a single crystal were used (data sets i1p, i1c), while in the other two the structure was refined simultaneously on data from two different crystals (data sets i3c and i6c). The final *R*1(obs) values ranged between 9.83% and 12.48%, with an average of 11.9%, *i.e.* around 8 percentage points improvement with respect to the kinematical results (Table 4). All refinements of

Table 3
Summary of the solution and refinement of natrolite structure.

In the last two rows the average agreement factors and their standard deviations (Stdev.) are reported.

Label	Lab	Data processing	Solution	Refinement	R_{int} (%)	Compl. (%), (resolution, Å)	Kinematical		Dynamical	
							R(obs)	*R*(all)	*R*(obs)	*R*(all)
n1p	1	*PETS2*	*Sir2019*	*OLEX2* (kin)/*Jana2020* (dyn)	17.55	85 (0.75)	15.44	18.47	9.21	12.76
n2c	2	*PETS2*	*Superflip*	*Jana2020*	10.71	97 (0.48)	19.60	21.25	13.61	14.15
n3p	3	*PETS2*	*Superflip*	*Jana2020*	12.80	95 (0.50)	14.36	15.68	6.63	10.35
n3c	3	*PETS2*	*Superflip*	*Jana2020*	19.44	95 (0.50)	16.95	17.11	5.74	5.92
n4p	4	*eADT*/*PETS2*	*Sir2014*	*ShelxL* + *OLEX2* (kin)/*Jana2020* (dyn)	13.25	99 (0.67)	13.98	14.84	12.27	15.97
n5c	5	*REDp*/*XDS*	*ShelxT*	*ShelxL*	19.10	88 (0.68)	13.67	15.87		
n6p	6	*PETS2*	*Superflip*	*Jana2020*	18.73	78 (0.66)	15.53	16.71	10.04	12.09
n7c	7	*DIALS*	*ShelxT*	*ShelxL*	18.29	73 (0.67)	15.98	18.59		
						Average	**15.69**	**17.32**	**9.58**	**11.87**
						Stdev.	**1.8**	**1.9**	**2.8**	**3.2**

S-ibuprofen were performed without any restraints or constraints except for the hydrogen atoms, which were refined in riding mode.

3.2. Lattice parameters

The determination of lattice parameters is an integral part of the structure determination. They are crucial for phase identification, and they are also an important indicator of the crystal system. Accurate lattice parameters are thus very important. It is a well known fact that lattice parameters determined from 3D ED data are significantly less accurate than those from X-ray diffraction methods. This discrepancy arises primarily from calibration errors, goniometer instabilities, optical distortions and, sometimes, radiation-damage-induced changes in the lattice parameters. Recent studies have shown that geometric distortions, including ED frame misorientations and optical distortions, can be corrected during data reduction (Brázda *et al.*, 2022). Additionally, calibration errors can be minimized by using an internal standard during data collection. When both conditions are met, high accuracy in lattice parameter determination can be achieved, as demonstrated in a recent study on oxide thin films (Passuti *et al.*, 2023).

All the 3D ED data in this article were collected using microscopes not exclusively dedicated to 3D ED, and are inevitably affected by both calibration errors and optical distortions. The large body of data sets coming from very diverse sources gives us a good opportunity to evaluate the typical accuracy of the lattice parameters. All data sets were used in the analysis except for e4p, n4p and i4p, for which accurate detector calibration was not available, and they could not be used for the analysis of the lattice parameters.

Tables S7, S9 and S11 summarize the lattice parameters of epidote, natrolite and ibuprofen, as determined from the 3D ED data, and their relative errors. Figs. S1, S2 and S3 show the scatterplots of the lattice parameters for each sample. The scatterplots in Figs. S1 and S2 show a visible correlation between the lattice parameters. They tend to be either all too large with respect to the reference value or all too small. The correlation arises due to the errors in the magnification calibration, which are almost inevitable in standard 3D ED experiments. To investigate other sources of errors than the magnification, we have also calculated the lattice parameters rescaled so that the unit-cell volume after rescaling equalled the unit-cell volume of the reference. These normalized lattice parameters are listed in supporting information, and they are also included in Figs. S1, S2 and S3.

For epidote, the average relative error is 1.05%, with the largest relative error of a lattice parameter being −3.35% (Table S7). This error comes from one of the three experiments with a clearly underestimated magnification calibration constant (e2c, e5c, e7c). After rescaling, the largest relative error drops to 1.12%, and the average relative error to only 0.27%. The error on the monoclinic angle reaches more than 1° in one case and 0.62° in another case, but in the remaining five refinements it was smaller than 0.09°.

Natrolite gives a similar picture. Interestingly, almost all data sets give overestimated lattice parameters. Without rescaling, the maximum relative error is 3.75%. This error comes from the data set n5c, which is a strong outlier (see the supporting information). The average relative error is 0.81%. After rescaling, the maximum error decreases to 1.94%, and with the outlier data set n5c excluded it is only 0.73%. The average relative error after rescaling is 0.39%, and with the n5c data set excluded, it amounts to only 0.25%.

The situation is quite different with ibuprofen. The number of available data sets is limited, but it is still clear that the lattice parameters refined from 3D ED tend to be systematically different from the X-ray reference, although they were measured at the same temperature. First, all lattice parameters are significantly larger than in the X-ray reference. The difference is so significant that it is probably real. But even after rescaling, there are systematic differences. The lattice parameter a tends to be longer in 3D ED data, while b is shorter, and c tends to be longer again (Fig. S3). There is no clear trend in the monoclinic angle β. Without rescaling, the maximum relative error is 2.88%, and the average is 1.62%. After rescaling, the values decrease to a maximum of 2.00% and an average of 0.60%. Despite the limited amount of data, it seems that the difference in the lattice parameters between the 3D ED and X-ray diffraction experiments does not arise

Table 4
Summary of the solution and refinement of the *S*-ibuprofen structure.

In the last two rows, the average agreement factors and their standard deviations (Stdev.) are reported.

Label	Lab	Data processing	Solution	Refinement	R_{int} (%)	Compl. (%), (resolution, Å)	Kinematical		Dynamical	
							R(obs)	*R*(all)	*R*(obs)	*R*(all)
i1c	1	*PETS2*	*ShelxT*	*OLEX2* (kin)/*Jana2020* (dyn)	27.99	72 (1.00)	21.73	27.87	12.22	16.24
i1p	1	*PETS2*	*ShelxT*	*OLEX2* (kin)/*Jana2020* (dyn)	27.32	70 (1.00)	17.57	24.96	10.27	26.75
i3c	3	*PETS2*	*Superflip*	*Jana2020*	15.45	85 (1.00)	18.28	22.52	10.49	16.10
i4p	4	*eADT/PETS2.0*	*Sir2014*	*ShelxL*	21.66	76 (0.83)	22.77	34.34		
i5c	5	*REDp/XDS*	*ShelxT*	*ShelxL*	39.04	98 (0.85)	15.88	21.20		
i6c	6	*PETS2*	*ShelxT*	*Jana2020*	18.57	60 (0.78)	21.84	27.08	12.48	17.36
						Average	**19.68**	**24.71**	**11.37**	**19.11**
						Stdev.	**2.6**	**4.3**	**1.0**	**4.4**

only from experimental errors, but it reflects a real difference. We can propose two reasons for this difference: it can be attributed partly to the different pressure (vacuum versus ambient pressure), but we think that the dominant reason is most likely the radiation damage inflicted on the crystal by the electron beam.

The overall conclusion from the analysis of the lattice parameters is that for the inorganic, beam-stable materials, the dominant source of error is the inaccuracy of magnification calibration, and rescaling the lattice parameters brings the typical relative error down to a small fraction of a per cent. This opens an interesting option for an improvement of the phase identification procedures using lattice parameters from 3D ED. The accuracy and sensitivity of phase identification could be improved if the lattice parameters were rescaled to the unit-cell volume of the reference phase before comparing the lattice parameters.

For beam-sensitive samples, the discrepancy of the lattice parameters may be systematic, arising from radiation damage or changes in the experimental conditions. In these cases, the comparison between 3D ED and X-ray lattice parameters should be done with caution.

3.3. Evaluation of the structure models

To check the accuracy of the 3D ED structure determination, single crystals from the same batches of samples were also studied by single-crystal X-ray diffraction. The instruments used were a Rigaku XtaLAB Synergy, equipped with an Mo source for the inorganic samples (Tables S4 and S5), and an Oxford Diffraction Supernova, equipped with a Cu source for *S*-ibuprofen at low temperature (Table S6). Details of the refinements are reported in the supporting information. As can be seen from the reported results, interestingly, among the inorganic samples, the hydrogen-atom positions could be determined only in natrolite and not in epidote, despite the good quality of the data and refinement. We used the X-ray refined structures as a reference for the comparison with the 3D ED results.

For the two inorganic structures, the comparison was carried out using the *COMPSTRU* utility of the Bilbao Crystallographic Server (de la Flor *et al.*, 2016), which delivers the distance between the corresponding atomic positions of the two compared structures. In *COMPSTRU*, 'the difference between the two models is quantified by evaluation of the global distortion decomposed into a spontaneous strain (lattice deformation) and atomic displacement field representing the distances between the paired atoms of the two structures' (see https://webbdcrista2.ehu.es/cryst/compstru.html). Therefore, before comparing the atomic positions of the checked structure with the reference one, the software deforms its unit cell to make it most similar to the reference, and then it evaluates the atomic shifts. So, if the atomic coordinates are very similar, but the unit cell is significantly different due to calibration and experimental deformation errors, the two structures will be similar anyway. Thus, the inaccuracy of the lattice parameters, discussed in Section 3.2, does not affect the comparison. As key parameters for the comparison, we considered the maximum (d_{max}) and the average (d_{ave}) distance to the atomic positions in the reference structure as given by *COMPSTRU*. The results of the comparison are reported in Tables 5, 6 and 7.

The hydrogen atoms were not considered in the comparison, since it is well known that the maximum of the electrostatic potential and of the electron density, the quantities responsible for electrons and X-ray scattering, respectively, are significantly shifted in the case of hydrogen (Gruza *et al.*, 2020; Nakane *et al.*, 2020; Klar *et al.*, 2023).

For epidote (Table 5), we observe good accuracy in the structure determination already in the kinematical refinement. One outlier exhibited a d_{max} of 0.120 Å and d_{ave} of 0.067 Å, while all other refinements had d_{max} below 0.075 and d_{ave} below 0.032. The dynamical refinement always visibly improved the structure model in both d_{max} and d_{ave}, bringing the average d_{ave} close to 0.01 Å, with the best result having a remarkably low average error of 0.004 Å.

Although the *R* values for natrolite are systematically lower than for epidote, the agreement between the refined structures and the X-ray model is similar to epidote (Table 6). Also in this case, we typically see an improvement between kinematical and dynamical refinement with respect to the X-ray model, although the improvement is less pronounced than in the case of epidote, with an average decrease of d_{ave} by 18%. This statistic is, however, somewhat distorted by the fact that some of the kinematical refinements already produced very accurate results, with little room for improvement in the

Table 5
Comparison between the 3D ED and the X-ray derived structures of epidote.

The average and standard deviation (Stdev.) over the results obtained by all laboratories are also listed.

	Kinematical		Dynamical		Fe	H-atom
Label	d_{max} (Å)	d_{ave} (Å)	d_{max} (Å)	d_{ave} (Å)	occupancy	detection
e1p	0.1199	0.0672	0.0499	0.0233	0.60 (4)	Yes
e2c	0.0740	0.0311	0.0116	0.0052	0.642 (14)	Yes
e3p	0.0439	0.0200	0.0106	0.0039	0.808 (10)	Yes
e3c	0.0443	0.0229	0.0143	0.0047	0.707 (12)	Yes
e4p	0.0482	0.0259	0.0372	0.0167	0.74 (4)	No
e5c	0.0321	0.0145			—	Yes
e6p	0.0427	0.0191	0.0329	0.0147	0.80 (2)	Yes
e7c	0.0584	0.0259			—	No
Average	**0.0579**	**0.0283**	**0.0260**	**0.0115**		
Stdev.	**0.026**	**0.015**	**0.015**	**0.007**	**0.08**	

Table 6
Comparison between the 3D ED and the X-ray derived structures of natrolite.

The average and standard deviation (Stdev.) over the results obtained by all laboratories are also listed. p.p. = percentage points.

	Kinematical		Dynamical		Enantiomorph	H-atom
Label	d_{max} (Å)	d_{ave} (Å)	d_{max} (Å)	d_{ave} (Å)	ΔR (p.p.)/z-score	detection
n1p	0.1220	0.0595	0.0580	0.0298	3.98/15.28	Yes
n2c	0.0605	0.0336	0.0182	0.0117	3.73/21.27	No
n3p	0.0244	0.0159	0.0222	0.0132	6.27/49.28	Yes
n3c	0.0180	0.0120	0.0185	0.0098	11.20/65.16	Yes
n4p	0.0256	0.0161	0.0478	0.0249	1.94/13.67	Yes
n5c	0.0514	0.0238				Yes
n6p	0.0321	0.0186	0.0295	0.0161	3.78/19.16	Yes
n7c	0.1895	0.0731				No
Average	**0.0592**	**0.0315**	**0.0323**	**0.0176**		
Stdev.	**0.056**	**0.021**	**0.15**	**0.007**	**2.98/19.5**	

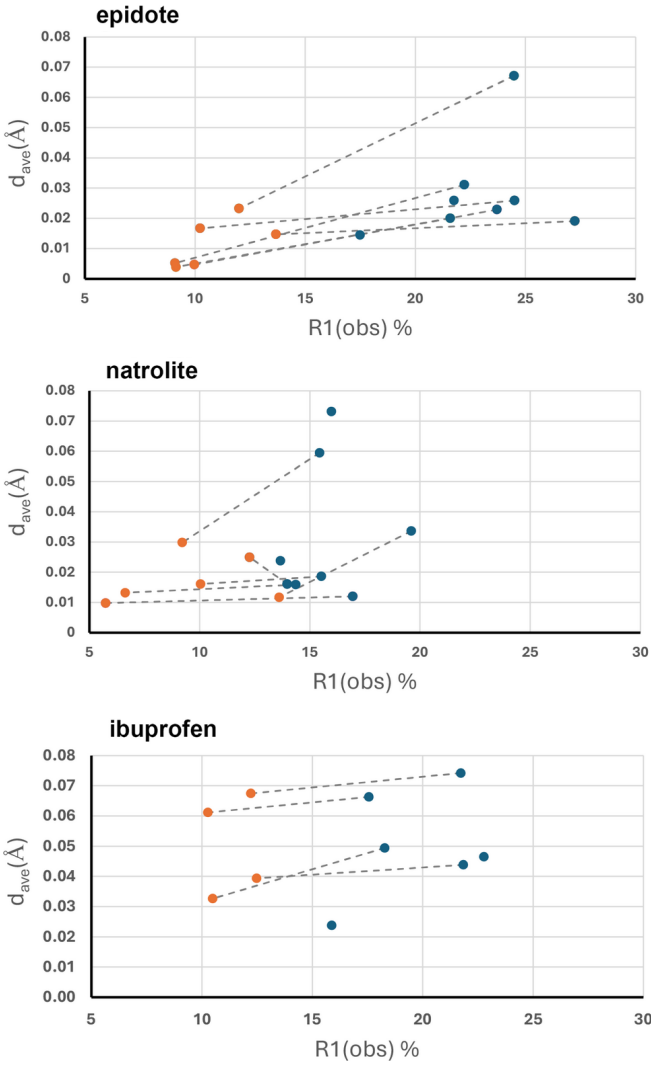

Figure 3
Plots of the average deviation from the reference structure versus the *R*1(obs) agreement factors of the refinements for epidote, natrolite and ibuprofen. Both kinematical (blue dots) and dynamical (orange dots) refinement data are reported. Dashed lines connect pairs of points corresponding to the kinematical and dynamical refinement from the same data.

dynamical refinement, and, in one of the six cases, d_{ave} increased from kinematical to dynamical refinement. In general, however, the accuracy remains very good, with an average distance of the atomic positions from the X-ray reference less than 0.02 Å.

It is difficult to compare organic structures between 3D ED and X-ray refinements. Very often, the molecules are slightly displaced between the two methods due to the effect of vacuum versus ambient pressure as well as the effects of radiation damage. As a result, a difference in atomic positions in a 3D ED structure with respect to the X-ray structure does not necessarily mean a lower accuracy of the 3D ED structure. However, the differences, in general, do not affect the covalent bond lengths, and these can be used to assess the accuracy of the structure. Moreover, the Cambridge Structural Database (CSD) contains a large number of structures, and the tool *Mogul* (Bruno *et al.*, 2004) can be used to compare any structure with the structures in the CSD. This allows assessment of the accuracy of a structure even in the absence of a reference structure. It should be noted that a deviation of a bond length from the average value in the database does not necessarily imply an error, but such cases are rare and usually easy to identify.

Table 7 summarizes the results of the evaluation of each structure with *Mogul*. The average bond-length deviation of all kinematical refinements is 0.050 Å. The typical maximum deviation is around 0.14 Å, although in one case the maximum deviation is as high as 0.28 Å. The dynamical refinement again provided an improvement of d_{ave} compared with the kinematical refinement in all cases, but this improvement can be considered minor. Overall, the average deviation of bond lengths in the dynamical refinements was 0.050 Å. For comparison, the same evaluation of the X-ray reference refinement yields an average deviation of 0.005 Å, *i.e.* about ten times lower. It is also worth noting that the best 3D ED result was obtained from the kinematical refinement on data set i5c, for which the data were obtained by merging data from ten crystals.

All the refinements and their accuracy are summarized in Figs. 3 and 4. In Fig. 3 we plot the average deviation of the

Table 7
Comparison of the *S*-ibuprofen structure with average distances in the CSD using *Mogul*.

d_{ave} is the average difference between the bond lengths in each refined structure from the average value found in the CSD for chemically equivalent bonds. d_{max} is the maximum difference among all bond lengths in each structure. The average and standard deviation (Stdev.) over the results obtained by all laboratories are also listed. p.p. = percentage points.

	Kinematical		Dynamical		Enantiomorph	H-atom
Label	d_{max} (Å)	d_{ave} (Å)	d_{max} (Å)	d_{ave} (Å)	ΔR (p.p.)/z-score	detection
i1c	0.278	0.074	0.207	0.067	3.07/5.11	13/34
i1p	0.181	0.066	0.205	0.061	1.53/5.75	12/34
i3c	0.122	0.049	0.120	0.033	1.28/8.49	19/34
i4p	0.130	0.047				No
i5c	0.058	0.024				20/34
i6c	0.105	0.044	0.097	0.039	2.18/6.08	15/34
Average	**0.146**	**0.051**	**0.157**	**0.050**		
Stdev.	**0.07**	**0.016**	**0.05**	**0.014**	**0.7/1.3**	
X-ray reference	0.016	0.005				

atom positions/bond lengths from the reference versus the agreement factors, while in Fig. 4 we directly compare through spider diagrams the different accuracy between the kinematical and dynamical refinements performed on the same data sets. Fig. 3 reveals some interesting trends. In the two inorganic samples, there is a good correlation between the value of $R1$ and d_{ave}, with the best $R1$ value also corresponding to the best d_{ave}. This correlation is clear for dynamical refinement, but not always true for the kinematical refinements. In ibuprofen, such correlation cannot be observed either in the kinematical or in the dynamical refinements, except for the refinement i5c obtained against ten data sets, which gives clearly the best $R1$(obs) value and also the best value of d_{ave}.

3.4. Specific challenges

3.4.1. Epidote

The first challenge for epidote is detecting the presence of hydrogen in the structure. This is primarily supported by bond valence sum (BVS) calculations (Brown, 2016), which indicate that a hydrogen atom is bound to oxygen sites with a formal valence of −1. This information can be immediately derived from most kinematical refinements. However, determining the exact position of a hydrogen atom in an inorganic structure is usually not straightforward from a kinematical refinement alone (Palatinus *et al.*, 2017). In the present case, one laboratory could pinpoint the hydrogen-atom position from a kinematical refinement by merging five different data sets, indicating that merging significantly improves the data quality, allowing subtle information to emerge. All six dynamical refinements could identify the hydrogen-atom position in the difference Fourier map (Fig. 5) and refine it. In three data sets (e1p, e2c and e6p) the hydrogen atom was refined with riding atomic displacement parameters (ADPs), but no restraints on the position, while in the other three (e3c, e3p, e4p) the hydrogen atom was refined completely freely, including the ADPs.

Determining the ratio between two chemical species present on the same atomic site (mixed occupancy) can be challenging using 3D ED and sometimes even with X-ray diffraction. This difficulty arises partly from the proximity of the elements in the periodic table: the closer the elements are, the more difficult the analysis. Furthermore, if one element is only marginally present, its presence may go unnoticed. In

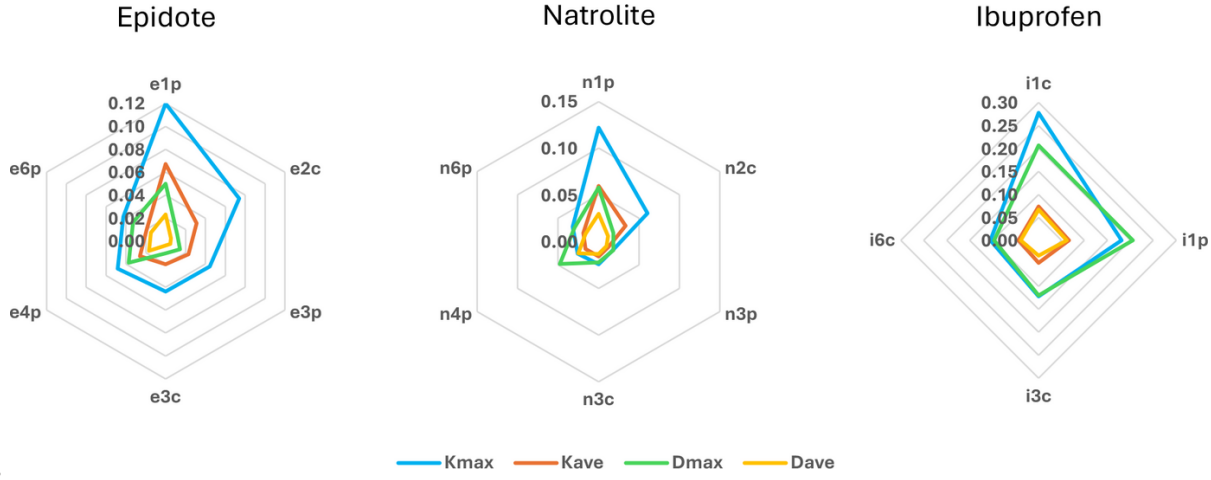

Figure 4
Spider diagrams showing a comparison between dynamical and kinematical refinement of the average and maximum deviation (in Å) from the reference structure for the three samples. K_{max} and K_{ave} refer to kinematical refinements while D_{max} and D_{ave} refer to dynamical refinements. The numbers that label the data collections correspond to the labs reported in the tables, while the final letters c or p indicate cRED or PEDT experiments, respectively.

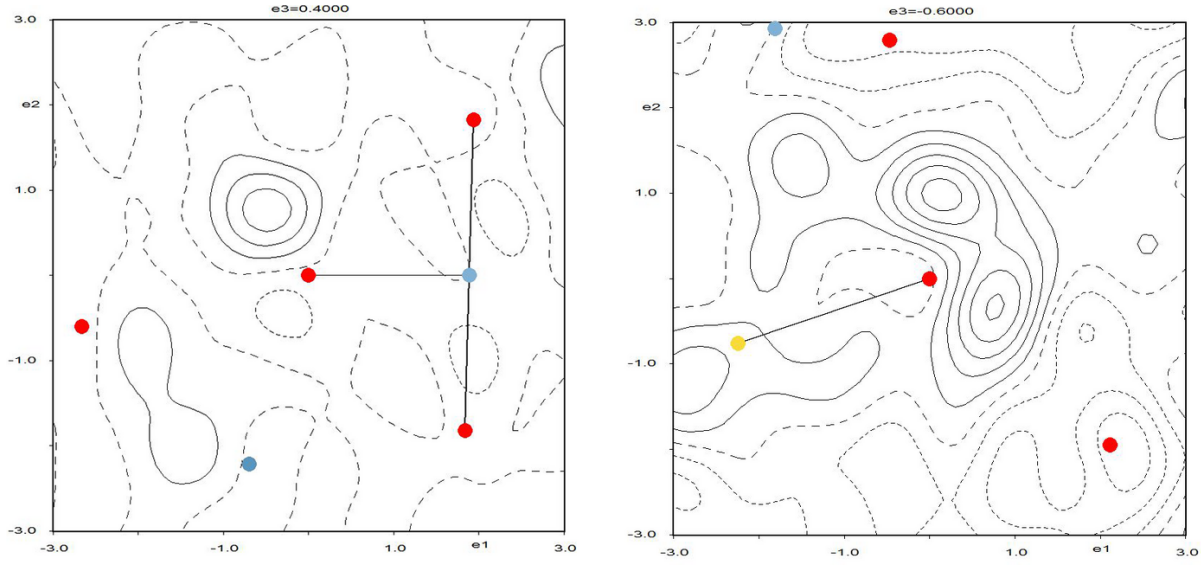

Figure 5
(Left) Fourier difference map calculated on an epidote data set refined dynamically before hydrogen-atom detection. The positive peak corresponding to the hydrogen of the hydroxyl group is clearly visible. Red points are O-atom positions, light-blue points are Al-atom positions. (Right) Fourier difference map calculated on a natrolite data set refined dynamically before the hydrogen-atom detection. Two positive peaks corresponding to the hydrogens of the water molecule are clearly visible. Red points are oxygen-atom positions, light-blue points are Al-atom positions, yellow points are Ca-atom positions.

such cases, another important factor to consider is the correlation between ADPs and atomic site occupancy. The marginal presence of either element can be accommodated by slight variations in ADPs. In this context, it is also worth noting that two kinematical refinements lead to non-positively defined isotropic ADPs (e1p_kin and e2c_kin), illustrating the difficulty of extracting meaningful ADPs from kinematical refinements and, consequently, of accurately determining sites with mixed occupancy or deficiencies. For these two data sets, dynamical refinements effectively resolve this issue, yielding positively defined ADPs.

For the mixed Fe/Al occupancy site in epidote, where Fe has twice the atomic number of Al and Al is significantly present, sufficient contrast is expected. This is demonstrated in X-ray diffraction on a single crystal (Table S4), where an Fe/Al ratio of 2:1 is established, with an occupancy of 0.67 Fe (0.33 Al). Concerning 3D ED data, five laboratories could refine the occupancy on six data sets, four PEDT and two cRED. For this, laboratories rely on dynamical refinements, which have already proven to deliver superior results (Palatinus *et al.*, 2015*a*; Palatinus *et al.*, 2017). The refined Fe occupancies range from 0.57 to 0.81. The average of the six values is quite close to the X-ray result, but the spread indicates that, even with good-quality data, the atomic occupancy is a difficult parameter to refine accurately, and the result of such a refinement should be interpreted with caution.

3.4.2. Natrolite

Determining the correct crystal system for natrolite can be challenging when relying solely on lattice parameter measurements. While experimental setups with minimal geometric distortions may correctly identify the orthorhombic cell, others may instead yield a tetragonal solution with $a \simeq 13.1$ Å and $c \simeq 6.6$ Å. This tetragonal model, assigned to space group $I\bar{4}2d$, represents a plausible structure in which the main difference is a mixed Al/Fe (50/50) occupancy at atomic sites corresponding to Si2 and Al1 in the orthorhombic model. To ensure reliable results, we recommend assessing geometric distortions using a well characterized reference material to establish the expected accuracy of the unit-cell parameters. Caution is also required when correcting geometric optical distortions. In *PETS2*, for example, selecting an inappropriate crystal system may cause the software to impose an incorrect symmetry and apply unsuitable corrections. When uncertainties remain, the examination of oriented zone-axis patterns can be decisive for space-group assignment, using static or precession-assisted parallel-beam electron diffraction or convergent beam electron diffraction (CBED). In the present case, the crystal system could be confidently assigned as orthorhombic based on the lattice parameters alone.

In all refinements except n7c, it was possible to distinguish between Si and Al atoms from the cation-to-oxygen distances of the three tetrahedral sites. In the case of Si, the average Si—O distances were always shorter than 1.67 Å while the average Al—O distances were longer than 1.73 Å (see the supporting information and Fig. 2). It is not clear why the kinematical refinement n7c does not provide sufficiently accurate distances. None of the indicators like $R1$ or R_{int} are exceptionally bad, although they are on the worse end of the ranges of the natrolite data sets.

The hydrogen atoms of the water molecules were detected in five out of six dynamically refined models (Table 6) and remarkably in one kinematically refined model, the one in which the intensities were from the merging of five data sets.

Dynamic effects in electron diffraction lead to the violation of Friedel's law and, in theory, grant 3D ED greater sensitivity than X-ray diffraction for determining the absolute structure of a compound or the absolute configuration of a molecule (Klar *et al.*, 2023). Kinematical refinements do not provide access to this information, and only dynamical refinements are capable of determining the absolute structure. Concerning the sensitivity to the absolute structure, all dynamical refinements provided a significant difference in the *R* values between the two enantiomorph structures (between 1.94 and 11.2 per cent point difference), as well as very high *z*-scores (between 13.7 and 65.2, Table 6), confirming that the determination of the absolute structure of an inorganic compound is easily possible.

3.4.3. *S*-ibuprofen

The ibuprofen sample proved to be a true challenge. Although hydrogen-atom detection in organic samples has slowly become almost routine for many 3D ED data sets, in the case of ibuprofen it turned out to be quite hard. For this work, we consider a hydrogen atom to be detected in the difference Fourier potential map if a maximum above 2.5σ close to the expected hydrogen-atom position is found in the difference potential map obtained after a free refinement of the structure without hydrogen atoms. Only between 12 and 19 hydrogen atoms out of 34 independent ones could be found in the four dynamical refinements, while, interestingly, 20 hydrogen atoms could be determined in the kinematical refinement i5c, indicating once again the excellent quality of the results obtained by merging data from multiple crystals.

The absolute structure determination again proved to be an easier task than hydrogen-atom detection. All four dynamical refinements of ibuprofen could determine the absolute structure with very good confidence levels (*z*-scores above 5).

4. Conclusions

The results of this round robin confirm that the 3D ED technique is sufficiently advanced to tackle the various challenges presented. These results were achieved by laboratories with both the instruments and expertise needed to address these challenges. However, it is important to note that the work presented here is primarily based on studies conducted by young PhD students. This work thus provides an estimate of the variability in the results that can be obtained by 3D ED under various conditions. For kinematical refinements, regardless of the instrument used or the operator, we observe that an average precision of 0.03 Å on the atomic positions is achieved for beam-resistant samples. This increases to 0.05 Å for beam-sensitive samples, which require rapid experiments under low-dose and cryogenic conditions. Dynamical refinement represents a significant advance in bridging the gap with X-ray diffraction. In most cases, it has improved the accuracy of atomic positions compared with kinematical refinement on the same data, reaching, on average, 0.01 Å for inorganic samples and 0.05 Å for the beam-sensitive sample. The agreement between calculated and observed intensities is also greatly improved, with *R* values reduced to a half of those obtained through kinematical refinements, typically falling within a range of 5% to 13%. This is particularly remarkable, especially considering that this level of precision could be achieved on potentially much smaller crystals than those studied here, and typically inaccessible to single-crystal X-ray diffraction. This is addressed in a study focused on the use of 3D ED for nanoparticles (Cordero Oyonarte *et al.*, 2025).

The improvement of the structural model achieved with the use of dynamical refinement is very clear for the two inorganic compounds, but not so pronounced for the organic compound. In the case of ibuprofen, the best result was actually obtained through kinematical refinement of ten merged data sets. Although further studies are needed to prove this more quantitatively, merging data from different crystals results in data closer to the kinematical condition, leading to better agreement factors and increased precision in the kinematical refinement. This point is particularly relevant for very fragile organic compounds, where approaches such as serial electron diffraction have already proven effective (Bücker *et al.*, 2020; Hogan-Lamarre *et al.*, 2024; Plana-Ruiz *et al.*, 2025) in obtaining reliable results by merging a series of single ED patterns collected from thousands of crystals. With data from a limited number of crystals, however, obtaining reliable and precise structural information from 3D ED data is more likely to be achievable through dynamical refinements. Dynamical refinement performs worse if the data quality is poor due to poor crystallinity. In fact, dynamical calculations assume a perfect crystal structure, an assumption that becomes less well valid in case of poorly crystalline organic compounds with large mosaicity. This effect can be seen on the ibuprofen sample, where the improvement of the dynamical refinement with respect to the kinematical one is less pronounced. In extreme cases, it may happen that the dynamical refinement does not improve the kinematical refinement at all. This is, however, not the case for ibuprofen, despite its relatively poor crystallinity and its sensitivity to the vacuum condition inside the TEM. Moreover, efforts to improve the dynamical refinement for the cases of imperfect crystals are ongoing and are bringing first promising results (Palatinus, 2024; Motaln *et al.*, 2025).

On top of the improved accuracy of the structure model, dynamical refinement has proven crucial for addressing the specific challenges of each structure. In particular, dynamical refinement was able to determine the absolute structure in both the inorganic and organic compounds.

A critical point appears to be the determination of the unit cell, which shows lower precision in our results compared with X-ray diffraction. While the results of the structure solution and refinements are typically not greatly impacted by the inaccuracy and variation in the unit-cell parameters, this point should be considered by newcomers to the field. The community, fully aware of this limitation, has made efforts to provide solutions to this issue. As mentioned in this article, it can be partly addressed by calibrating the instrument more rigorously (including using an internal standard for each experiment) and correcting for geometric distortions induced

by the microscope goniometer and optics during data reduction. However, these practices are not consistently used by the laboratories that took part in this study, leading to variability in the results. In this context, dedicated instruments, such as the recently introduced electron diffractometers, could improve these results. Having instruments without projection lenses, where the camera length is finely calibrated and kept fixed, should, in principle, improve the accuracy of the unit cell to below 0.1% in lengths and 0.1° in angles. For organic and other beam-sensitive samples, however, a change of lattice parameters due to radiation damage can always be expected.

The beam-sensitive organic sample was specifically chosen as an extreme case where both vacuum and beam sensitivity were critical. Although the challenges of the sample slightly worsened the accuracy, all the laboratories equipped with a cryo-holder succeeded in determining the structure. In conclusion, the round robin demonstrates that 3D ED has reached a level of stability in both the methodology of data collection and data analysis that makes the results reproducible independently of the instrument used, and the structure solution and refinement reliable across a wide spectrum of samples. Nevertheless, careful analysis is still needed to avoid errors and bias in the resulting structure model.

Funding information

This research was supported by the European Union's Horizon 2020 research and innovation programme under the Marie Skłodowska-Curie grant agreement No. 956099 (NanED – Electron Nanocrystallography – H2020-MSCAITN).

References

Brázda, P., Klementová, M., Krysiak, Y. & Palatinus, L. (2022). *IUCrJ* **9**, 735–755.
Brown, I. D. (2016). *The chemical bond in inorganic chemistry: the bond valence model*, 2nd ed. Oxford University Press.
Bruno, I. J., Cole, J. C., Kessler, M., Luo, J., Motherwell, W. D. S., Purkis, L. H., Smith, B. R., Taylor, R., Cooper, R. I., Harris, S. E. & Orpen, A. G. (2004). *J. Chem. Inf. Comput. Sci.* **44**, 2133–2144.
Bücker, R., Hogan-Lamarre, P., Mehrabi, P., Schulz, E. C., Bultema, L. A., Gevorkov, Y., Brehm, W., Yefanov, O., Oberthür, D., Kassier, G. H. & Dwayne Miller, R. J. (2020). *Nat. Commun.* **11**, 996.
Burla, M. C., Caliandro, R., Carrozzini, B., Cascarano, G. L., Cuocci, C., Giacovazzo, C., Mallamo, M., Mazzone, A. & Polidori, G. (2015). *J. Appl. Cryst.* **48**, 306–309.
Clabbers, M. T. B., Gruene, T., Parkhurst, J. M., Abrahams, J. P. & Waterman, D. G. (2018). *Acta Cryst.* D**74**, 506–518.
Cordero Oyonarte, E., Rebecchi, L., Gholam, S., Faye Diouf, M. F., Bigard, E., Pralong, V., Prestipino, C., Kriegel, I., Castellanos-Aliaga, A., Hadermann, J., Gemmi, M., Palatinus, L., Plaisier, J. L. & Boullay, P. (2025). *ACS Nano* **19**, 20599–20612.
de la Flor, G., Orobengoa, D., Tasci, E., Perez-Mato, J. M. & Aroyo, M. I. (2016). *J. Appl. Cryst.* **49**, 653–664.
Dollase, W. A. (1971). *Am. Mineral.* **56**, 447–464.
Dolomanov, O. V., Bourhis, L. J., Gildea, R. J., Howard, J. A. K. & Puschmann, H. (2009). *J. Appl. Cryst.* **42**, 339–341.
Freer, A. A., Bunyan, J. M., Shankland, N. & Sheen, D. B. (1993). *Acta Cryst.* C**49**, 1378–1380.
Gemmi, M., La Placa, M. G. I., Galanis, A. S., Rauch, E. F. & Nicolopoulos, S. (2015). *J. Appl. Cryst.* **48**, 718–727.
Gemmi, M., Mugnaioli, E., Gorelik, T. E., Kolb, U., Palatinus, L., Boullay, P., Hovmöller, S. & Abrahams, J. P. (2019). *ACS Cent. Sci.* **5**, 1315–1329.
Gruza, B., Chodkiewicz, M. L., Krzeszczakowska, J. & Dominiak, P. M. (2020). *Acta Cryst.* A**76**, 92–109.
Hogan-Lamarre, P., Luo, Y., Bücker, R., Dwayne Miller, R. J. & Zou, X. (2024). *IUCrJ* **11**, 62–72.
Ito, S., White, F. J., Okunishi, E., Aoyama, Y., Yamano, A., Sato, H., Ferrara, J. D., Jasnowski, M. & Meyer, M. (2021). *CrystEngComm* **23**, 8622–8630.
Kabsch, W. (2010). *Acta Cryst.* D**66**, 125–132.
Khouchen, M., Klar, P. B., Chintakindi, H., Suresh, A. & Palatinus, L. (2023). *Acta Cryst.* A**79**, 427–439.
Klar, P. B., Krysiak, Y., Xu, H., Steciuk, G., Cho, J., Zou, X. & Palatinus, L. (2023). *Nat. Chem.* **15**, 848–855.
Kolb, U., Gorelik, T., Kübel, C., Otten, M. T. & Hubert, D. (2007). *Ultramicroscopy* **107**, 507–513.
McConnell, J. F. (1974). *Cryst. Struct. Commun.* **3**, 73–75.
Meier, W. M. (1960). *Z. Kristallogr.* **113**, 430–444.
Momma, K. & Izumi, F. (2011). *J. Appl. Cryst.* **44**, 1272–1276.
Motaln, K., Gurung, K., Dragomir, M., Kurzydłowski, D., Palatinus, L. & Lozinšek, M. (2025). *Inorg. Chem.* **64**, 14968–14976.
Mugnaioli, E., Gorelik, T. & Kolb, U. (2009). *Ultramicroscopy* **109**, 758–765.
Nakane, T., Kotecha, A., Sente, A., McMullan, G., Masiulis, S., Brown, P. M. G. E., Grigoras, I. T., Malinauskaite, L., Malinauskas, T., Miehling, J., Uchański, T., Yu, L., Karia, D., Pechnikova, E. V., de Jong, E., Keizer, J., Bischoff, M., McCormack, J., Tiemeijer, P., Hardwick, S. W., Chirgadze, D. Y., Murshudov, G., Aricescu, A. R. & Scheres, S. H. W. (2020). *Nature* **587**, 152–156.
Nannenga, B. L., Shi, D., Leslie, A. G. W. & Gonen, T. (2014). *Nat. Methods* **11**, 927–930.
Nederlof, I., van Genderen, E., Li, Y.-W. & Abrahams, J. P. (2013). *Acta Cryst.* D**69**, 1223–1230.
Palatinus, L. (2024). *Acta Cryst.* A**80**, e225.
Palatinus, L., Brázda, P., Boullay, P., Perez, O., Klementová, M., Petit, S., Eigner, V., Zaarour, M. & Mintova, S. (2017). *Science* **355**, 166–169.
Palatinus, L., Brázda, P., Jelínek, M., Hrdá, J., Steciuk, G. & Klementová, M. (2019). *Acta Cryst.* B**75**, 512–522.
Palatinus, L. & Chapuis, G. (2007). *J. Appl. Cryst.* **40**, 786–790.
Palatinus, L., Corrêa, C. A., Steciuk, G., Jacob, D., Roussel, P., Boullay, P., Klementová, M., Gemmi, M., Kopeček, J., Domeneghetti, M. C., Cámara, F. & Petříček, V. (2015*a*). *Acta Cryst.* B**71**, 740–751.
Palatinus, L., Petříček, V. & Corrêa, C. A. (2015*b*). *Acta Cryst.* A**71**, 235–244.
Passuti, S., Varignon, J., David, A. & Boullay, P. (2023). *Symmetry* **15**, 1459.
Petříček, V., Palatinus, L., Plášil, J. & Dušek, M. (2023). *Z. Kristallogr. Cryst. Mater.* **238**, 271–282.
Plana-Ruiz, S., Lu, P., Ummethala, G. & Dunin-Borkowski, R. E. (2025). *J. Appl. Cryst.* **58**, 1249–1260.
Service, R. F. (2018). *Science* **362**, 1350.
Sheldrick, G. M. (2015*a*). *Acta Cryst.* C**71**, 3–8.
Sheldrick, G. M. (2015*b*). *Acta Cryst.* A**71**, 3–8.
Simoncic, P., Romeijn, E., Hovestreydt, E., Steinfeld, G., Santiso-Quiñones, G. & Merkelbach, J. (2023). *Acta Cryst.* E**79**, 410–422.
Tinti, G., Fröjdh, E., van Genderen, E., Gruene, T., Schmitt, B., de Winter, D. A., Weckhuysen, B. M. & Abrahams, J. P. (2018). *IUCrJ* **5**, 190–199.
Vincent, R. & Midgley, P. A. (1994). *Ultramicroscopy* **53**, 271–282.
Vypritskaia, A., Zou, X., Yang, T. & Waterman, D. G. (2025). *Acta Cryst.* C**81**, 1–13.
Winter, G., Waterman, D. G., Parkhurst, J. M., Brewster, A. S., Gildea, R. J., Gerstel, M., Fuentes-Montero, L., Vollmar, M., Michels-Clark, T., Young, I. D., Sauter, N. K. & Evans, G. (2018). *Acta Cryst.* D**74**, 85–97.